

## Airflow Patterns in Both Sides of a Realistic Human Nasal Cavity for Laminar and Turbulent Conditions

J.Wen<sup>1</sup>, K.Inthavong<sup>1</sup>, Z.F.Tian<sup>1</sup>, J.Y.Tu<sup>1</sup>, C.L.Xue<sup>2</sup> and C.G.Li<sup>2</sup>

<sup>1</sup>School of Aerospace, Mechanical and Manufacturing Engineering, RMIT University, Melbourne, VIC, 3083, Australia

<sup>2</sup>School of Health Sciences, RMIT University, Melbourne, VIC, 3083, Australia

### Abstract

Detailed data of air flow patterns can assist in the understanding of the physiological and pathological aspects of nasal breathing as well as the prediction of gas-particle flows. A computational model of a human nasal cavity was constructed from CT scans and air flow rates of 7.5L/min and 40L/min were simulated. The study obtained air flow patterns and its features such as pressure drop and airflow distribution and profiles for the left and right nasal cavities. The results were compared with each other while some results were compared with experimental and numerical data that were available. The flow patterns in the nasal valve and turbinate were studied in particular detail, since the airflow profiles in these regions have not been well investigated. Maximum velocities were found at the narrowest cross-sections at the nasal valve region. The airflow distribution showed airflow remaining close to the nasal septum wall and little flow reached the outer meatus regions. The role of the turbinates with respect to the airflow distribution and the possible health implications on the differences in the left and right cavities was briefly discussed.

### Introduction

The human nasal cavity is an important component to the respiratory system, which performs a variety of physiological functions. Besides respiration, it is responsible for heating and humidifying inspired air to near body core temperature and full saturation, while filtering the air from pollutants and toxic particles such as pollen, or exhaust fumes that may enter the airway. On the other hand, the airway provides an alternative route for drug delivery. Deposition sites on the highly vascularised mucosal walls provide improved speed of pharmacological action and retention of the drug composition, which is often destroyed when drugs are administered orally [8]. Detailed air flow patterns can provide data that is pertinent to the prediction of gas-particle flows and also regional tissue exposure to inhaled air that are found in toxicology and therapeutic inhalation studies. The numerical data which can produce highly quantitative results ideally complements existing experimental data that often lack fine details.

Airflow profiles in the human nasal passages have been studied experimentally by a number of researchers. Kelly et al. [10] investigated two-dimensional velocity fields in parallel planes to the flow direction, throughout a nasal cavity model using particle image velocimetry. Hahn et al. [6] used hot-film anemometer probe to measure the velocity distributions on five cross sections of an enlarged human nasal cavity model. In these experiments the flow was considered laminar up to breathing rate of 24 L/min. It was also reported that approximately half of the inspired airflow passed through the middle and inferior airways and a small fraction of the flow passed through olfactory slit. Churchill et al. [4] studied airflow patterns using water and dye

flowing through anatomically accurate acrylic models of ten different human nasal cavities. It was found that the nasal morphological features such as the inferior orientation of the nostrils, the relative size of the nasal valve, and the height of the nasal sill did not show statistically significant correlations among the ten models. However one parameter, the projection of the turbinate bones into the nasal cavity was shown to laminate the flow. These studies provide valuable descriptions of airflow patterns in the nasal passages of different individuals; however, quantitative detailed information regarding the airflow was limited.

Recent developments in medical imaging (MRI and CT scanning) coupled with computational science have opened new possibilities for physically realistic numerical simulations of nasal air flow. Numerical simulations of the human nasal airflow have been conducted by a few researchers. Keyhani et al. [11] examined airflow through one side of the human nose in a three-dimensional model that was truncated anterior to the nasopharynx. Subramaniam et al. [18] simulated the airflow structures of rest and light breathing conditions (15L/min and 26L/min) using a laminar flow. In these studies, flow through both nostrils were performed however the air flow patterns on both sides were not compared. Other airflow studies include the work by Zamanakham et al. [22] and Wang et al. [19] which briefly discussed airflows through one nasal cavity only.

The main factors that attribute to the airflow patterns are the nasal cavity geometry and the flow rate. For a realistic human nasal cavity, the left and right sides of the nasal cavity can differ in the geometric construction while nasal morphology differences can be found between individuals. Additionally the inspiratory flow rates for adults can range between 5-12L/min for light breathing and 12-40L/min for non-normal conditions such as during exertion and physical exercise. Usually the breathing switches from pure nasal flow to oral-nasal flow at this higher range. Additionally extreme forced inhalation conditions have been found to reach flow rates of 150 L/min (Robert [15]).

This study presents the flow phenomena inside the human nasal cavity in detail through CFD methods for a steady-state flow. CFD methods are advantageous in its ability to provide detailed data that is typically difficult to produce through experiments due to intervention and clinical risks for the volunteer. The study obtained air flow patterns and features, such as pressure drop and airflow distribution and profiles in both nasal cavities at flow rates of 7.5 L/min and 40 L/min. The according Reynolds number at the nostril is about 545 and 2905, respectively. The results for both nasal cavities were compared with each other while some results were compared with experimental and numerical data that were available in the literature. The flow patterns in the nasal valve and turbinate were studied in particular detail, since the airflow profiles in these regions have not been well investigated.

**Nasal Anatomy**

The nose is divided axially (along its long axis) into four regions: the vestibule, the nasal valve, the turbinate and the nasopharynx regions. In following descriptions, the +X coordinate axis is from the anterior tip of the nostril inlet to the nasopharynx which is referred to as the axial direction. The first three-quarters of the nasal cavity is divided into two cavities by the nasal septum. Air enters each cavity through the oval shaped external nostrils into the vestibule (Figure 1). The flow changes direction, 90° towards the horizontal, before entering the nasal valve region. In this region the airway is the narrowest causing an acceleration of the air. At the end of the nasal valve region the cross-sectional area of the airway increases suddenly. This expansion is the beginning of the turbinate region where the profile is complicated and asymmetrical. Finally, at the nasopharyngeal region, the left and right cavities merge together causing the flow in this region will mix together.

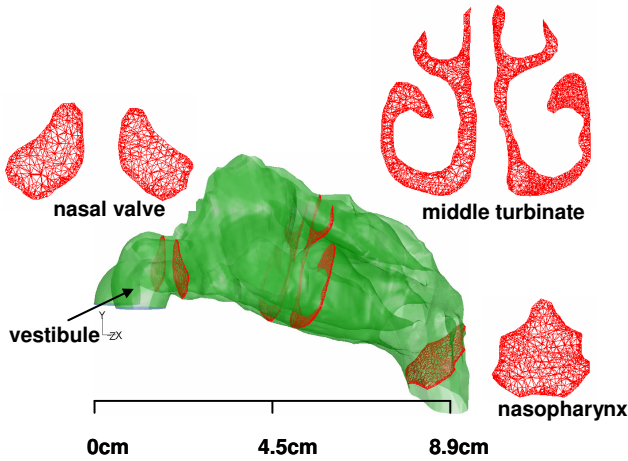


Figure 1. Nasal cavity model used in the study. Cross-sectional areas taken at the nasal valve, middle turbinate and nasopharynx regions are shown with the computational mesh.

**Methods**

**Grid Generation and Independent**

The nasal cavity geometry was obtained through a CT scan of the nose of a healthy 25 year old, Asian male (170 cm height, 75 kg mass). The CT scan was performed using a CTI Whole Body Scanner (General Electric). The single-matrix scanner was used in helical mode with 1-mm collimation, a 40-cm field of view, 120 kV peak and 200 mA. The scans captured outlined slices in the X-Y plane at different positions along the Z-axis from the entrance of the nasal cavity to just anterior of the larynx at intervals of 1 to 5 mm depending on the complexity of the anatomy. The coronal sectioned scans were imported into a three-dimensional (3D) modelling program called GAMBIT (GAMBIT 2.2, 2004) which created smooth curves that connected points on the coronal sections.

Stitched surfaces were then created to form a complete computational mesh. Because the details of the flow velocity and pressure were not known prior to solution of the flow problem, the outlet boundary condition is defined as an outflow with zero diffusion flux for all flow variables in the direction normal to the exit plane. This implies that the flow characteristics have to be consistent with a fully-developed flow assumption and a straight extension of the outlet plane was created into the geometry to satisfy this criterion.

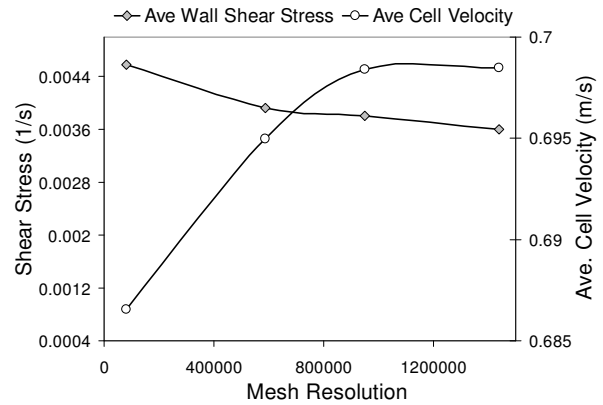


Figure 2. Shear stress and velocity profiles of a coronal section near the nasal valve region for the four different cavity models.

An initial model with 82,000 unstructured tetrahedral cells was initially used to solve the air flow field at a flow rate of 10L/min. The model was then improved by cell adaptation techniques that included refining large volume cells, cells that displayed high velocity gradients and near wall refinements, where a model with a higher cell count was produced. This process was repeated twice, with each repeat producing a model with a higher cell count than the previous model. Subsequently four models were produced, 82000, 586000, 950000 and 1.44million cells. A grid independence test shown in Figure 2, found the results for average velocity and the wall shear stress converge as the mesh resolution approached 950,000 cells. In order to make a compromise between the result's accuracy and computational cost, a model with 950,000 elements was used in this study (Figure 2).

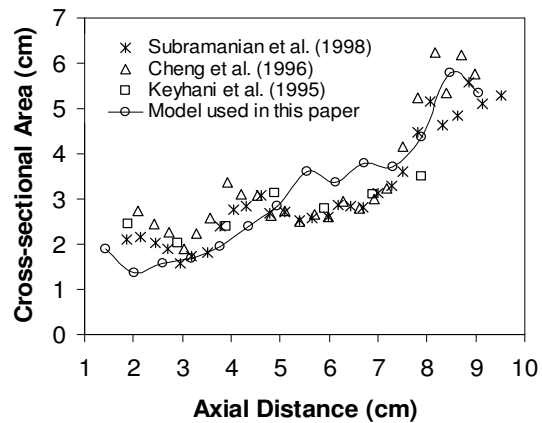


Figure 3 Comparison of cross-sectional areas versus distance from anterior tip of nose for different geometries: the cross-sectional area of both sides for different geometries.

The present computational model was compared with other nasal cavities where existing data was available. Although there exists inter-subject variations in nasal cavity geometries, a general trend can be observed on a macro level. For example a local minimum is found for all profiles just after the inlet where the nasal valve region exists. The nasal valve is the narrowest region where the cross-sectional area was found to be 1.4cm<sup>2</sup> which compares with 1.6 cm<sup>2</sup>, 1.9 cm<sup>2</sup> and 2.0 cm for Subramanian et al. [18], Cheng et al. [3] and Keyhani et al. [11]'s models respectively. At the anterior turbinate region the airway expands to accommodate the olfactory sensors and the turbinate bone projections. This is reflected where an increase in the cross-sectional profiles is observed immediately after the nasal valve

region. The nasal cavity model used in the present study exhibited the smallest cross-sectional area for the nasal valve region but had the largest cross-sectional area in the turbinate region when compared with other models. The overall length of the current model in the axial direction is also shorter in comparison. For the current geometry, the narrowest part in the region of valve is located about 2.0 cm from the anterior tip of nose, while that of Subramanian et al. (1998)[18], Cheng et al. (1995)[3] and Keyhani et al. (1995) [11] are all about 3.0 cm away from the anterior tip of nose. In summary the main distinctions of the nasal cavity used in this paper are a narrower nasal valve, wider turbinates and a shorter length in comparison with other models. These features will provide significant differences in the airflow and pressure distribution patterns.

### Gas Phase Modelling

A laminar model and the low-Reynolds number  $k-\omega$  turbulent model were used to simulate the flow field at flow rates of 7.5L/min and 40 L/min, respectively. The steady-state Navier-Stokes equations were employed to describe the laminar flow whilst the Reynolds Averaged Navier-Stokes (RANS) approach was used for the turbulent flow. The RANS approach was chosen as it is a more viable option over direct numerical simulations (DNS) to account for small scale, high frequency velocity fluctuations within the flow field. The low-Reynolds-number  $k-\omega$  turbulence model originally by Wilcox [21] has shown to be appropriate for simulating low-Reynolds-number turbulent internal flows mainly through the correction of the turbulent viscosity and its acceptable handling of shear flows and swirling flow. Additionally Bardina et al. [2] also proved that the LRN  $k-\omega$  model predicts the behaviour of attached boundary layers in adverse pressure gradients that occur at expansions in the flow, more accurately than the  $k-\epsilon$  model. The continuity equation for the incompressible gas phase (air) in Cartesian tensor notation is:

$$\frac{\partial}{\partial x_i}(\rho u_i) = 0 \quad (1)$$

where  $u_i$  is the  $i$ -th component of the time averaged velocity vector and  $\rho$  is the air density.

The momentum equation is given as:

$$\rho u_j \frac{\partial u_i}{\partial x_j} = -\frac{\partial p}{\partial x_i} + \frac{\partial}{\partial x_j} \left( \mu \frac{\partial u_i}{\partial x_j} \right) + \frac{\partial}{\partial x_j} \left( -\overline{\rho u_i u_j} \right) \quad (2)$$

where  $p$  is the gas pressure,  $\mu$  is the gas viscosity and  $-\overline{\rho u_i u_j}$  is the Reynolds Stress. Two further transport equations for the turbulence kinetic energy,  $k$ , and the dissipation rate,  $\omega$  are produced to close the model equations.

$$\frac{\partial}{\partial x_i} (p k u_i) = \frac{\partial^2 k}{\partial x_j^2} \left( \mu + \frac{\mu_t}{\sigma_k} \right) - \mu_t 2S^2 - \rho \beta^* k \omega + S_k \quad (3)$$

$$\frac{\partial}{\partial x_i} (p \omega) = \frac{\partial^2 \omega}{\partial x_j^2} \left( \mu + \frac{\mu_t}{\sigma_\omega} \right) - \frac{\alpha}{V_t} \mu_t 2S^2 - \rho \beta \omega^2 + S_\omega \quad (4)$$

where  $\sigma_k$  and  $\sigma_\omega$  are the turbulent Prandtl numbers for  $k$  and  $\omega$ , respectively and  $\beta$  is a function of the model constants. The low-Reynolds-number correction is included in the relation for  $\alpha$  and the Reynolds Stresses from Eqn.(3) are resolved by the Boussinesq assumption to produce the strain rate tensor,  $S$ . The model constants are defined by Wilcox [21] as  $C_\mu = 0.09$ ,  $\alpha = 0.555$ ,  $\beta = 0.8333$ ,  $\beta^* = 1$  and  $\sigma_k = \sigma_\omega = 0.5$ . Further details about the  $k-\omega$  model can be found in Wilcox [21].

Due to the complex geometry of the anatomically real nasal cavity, a commercial CFD code, FLUENT, was utilised to predict

the continuum gas phase flow under steady-state conditions through solutions of the conservation equations of mass and momentum. A pressure-based solver approach was undertaken for its better handling of low-speed incompressible flows. In this approach the pressure field is extracted by solving a pressure-correction equation obtained from the SIMPLE pressure-velocity coupling scheme. The discretisation of the unstructured tetrahedral mesh used a second-order-upwind scheme in order to obtain sufficiently accurate solutions. For a stable and accurate iterative process, the under-relaxation factors for momentum and pressure were initially set to 0.5 and 0.2 respectively which were subject to changes depending on the solution which was monitored. In addition, the residual values of the governing equations and the transport equations ( $k-\omega$ ) were all set to converge at  $10^{-5}$ .

### Airflow Conditions

The critical flow rate at which the flow changes from a laminar to a turbulent flow regime cannot be succinctly defined due to the complexity of the airway. There has been some debate concerning the type of airflow regime to implement for numerical simulations. Experimental studies by Bridger and Proctor [1] and Kelly et al. [10] have suggested that a laminar flow regime dominates for low flow rates around 10L/min. While Hahn et al. [6]'s results also concur, it is mentioned that the flow is a disturbed laminar regime. The work by Churchill et al. [4] found that the average rate at which flow switched from transitional to turbulent was 11L/min  $\pm$  5 (standard error). Despite this a survey of more recent numerical simulations of realistic nasal airways show a consensus among researchers in using a laminar flow for flow rates less than 20L/min.

Researcher	LPM (peak)	Viscous model
Keyhani al. [11]	12	Laminar
Zamankhan al. [22]	14	Laminar
Naftali et al. [13]	15	Laminar
Schroeter et al. [17]	15	Laminar
Inthavong et al. [9]	20	Turbulent
Pless et al. [14]	30	Turbulent
Lindemann et al. [12]	36	Turbulent
Weinhold and Mlynski [20]	12 – 84	Turbulent

Table 1. Literature survey of airflow simulations and the viscous models implemented.

## Results and Discussion

### Validation

The average pressure drop across the nasal cavity from the nostril inlet to nasopharynx was obtained at flow rates from 7.5 L/min to 40 L/min (Figure 4). The numerical results found good agreement with reported experimental data especially at flow rates less than 20 L/min. There is slight discrepancy of results for a flow rate of 40L/min. across all three models. The differences may be attributed to some experimental uncertainties as well as inter-subject variability between the nasal cavity models as shown in Figure 1. Therefore, when neglecting the experimental uncertainties and differences in geometry, the characteristics of the CFD results correspond to other models reasonably well over the entire range.

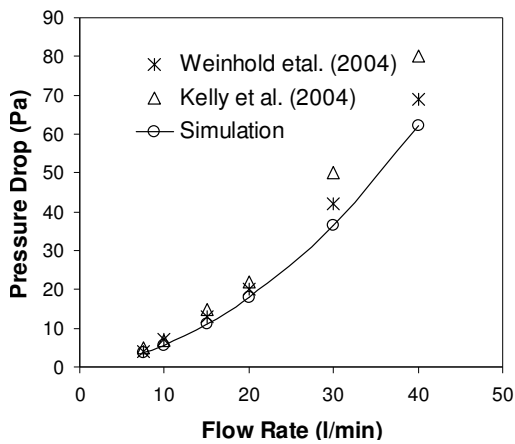
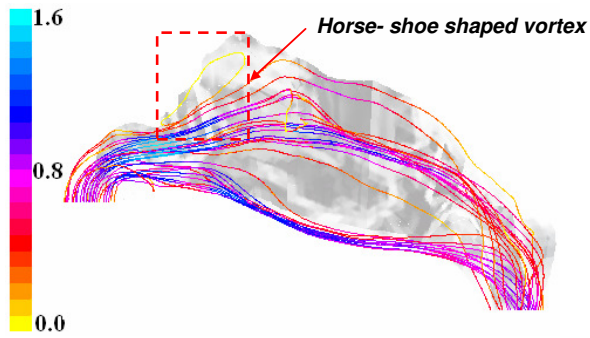
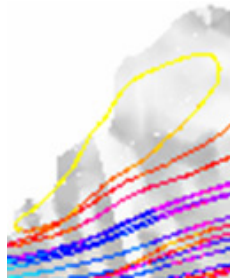


Figure 4. Pressure drop across the human nasal cavity as a function of inspiratory flow rate compared with reported experimental data.

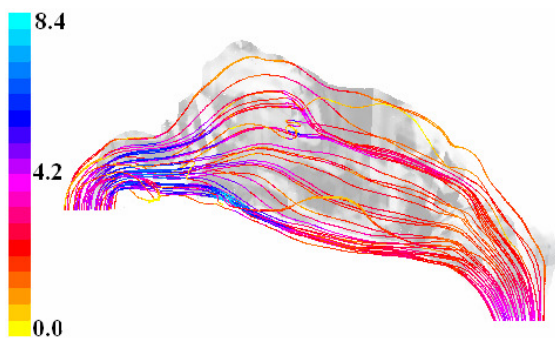
**Flow stream patterns**



(a) 7.5 L/min, Left



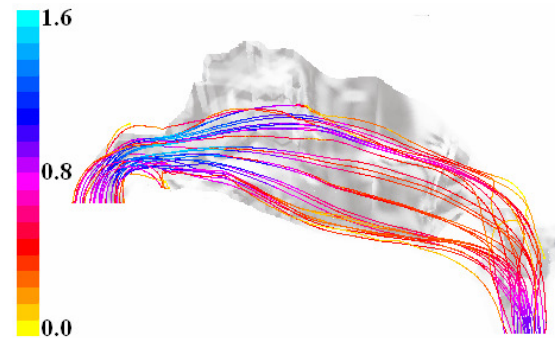
(b) Magnified view of Horse-shoe shaped vortex



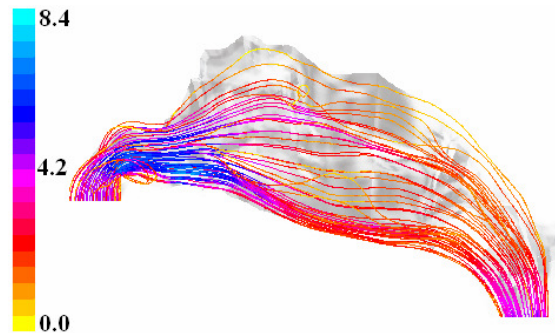
(c) 40 L/min, Left

Figure 5. Flow streamlines for the left nasal cavity at a flow rate of 7.5 L/min and 40 L/min Representation of flow streamlines in the nasal cavity at different flow rates.

Flow streamlines were captured by tracking the path traversed by a massless particle released from the inlet of each cavity which provides a qualitative visualization of the flow field. Airflow patterns for the left nasal cavity at a flow rate of 7.5 L/min (Figure 5a) show flow separation and reversed flow in the upper regions of the airway which is the location of the olfactory sensors, just posterior to the nasal valve. The horse-shoe shaped vortex is a result of the adverse pressure gradient caused by the abrupt increase in cross-sectional area from the nasal valve to the main nasal passage (Figure 5b). This feature was also found in the model of Weinhold et al. [20] who recorded this phenomenon on video as well as the model by Kelly et al. (2000) [10], through PIV images.



(a) 7.5 L/min, Right



(b) 40 L/min, Right

Figure 6. Flow streamlines for the right nasal cavity at a flow rate of 7.5 L/min and 40 L/min Representation of flow streamlines in the nasal cavity at different flow rates.

A majority of the flow is found to flow along the floor of the airway and another larger proportion flows around the mid-height level through the airway, a similar feature also found with that of Kelly et al. [10] and Hahn et al. [6]. In comparison with a higher flowrate of 40L/min, (Figure 5c) the streamlines of the same cavity show a more even distribution of streamlines which may be attributed to the higher velocities, enhanced mixing and a more even velocity distribution which is common for turbulent flows. Regions of recirculation are found in the superior turbinate region and near the nasal valve region where the constriction accelerates the flow through. In comparison with the right cavity the streamlines for a flow rate of 7.5 L/min were concentrated in the middle and lower regions (Figure 6). There is no streamline passing through the upper cavity. As the flow rate increased to 40 L/min, the streamlines are distributed more evenly. These results demonstrate that the flow patterns in the nasal cavity are sensitive to the anatomic geometry and flow rate.

The cross-section at the nasal valve region as depicted in Figure 1 was chosen for further analysis since this region showed high velocities. The naming convention used in this paper for the left and right cavity takes on the side that the cavity sits anatomically. The cross-section shown in Figure 6 is from a front on perspective and therefore the right cavity is depicted on the left side. The air enters the vestibule region with a vertical direction. As the distance increases from the anterior tip of the nostrils, the nasal geometry becomes thinner and narrow as it changes the direction of the transported air from vertical to horizontal. This transition coupled with the narrowing geometry forces a majority of the flow direction to come from the opposite side of the septum walls. The presence of the wall restricts the flow and forces the flow to recirculate thus formulating the vortices found in the right cavity (Figure 7). Two local vortices are found on the right cavity and one in the left and the direction of the vortices all point to the vortex centre, which represents a positive velocity gradient along the axial direction ( $X$ -direction) [5]. At a higher flow rate of 40L/min the location and nature of the vortices change in the right cavity. The upper vortex labelled vortex A shows the outer streamlines of the vortex directed inwards while the inner streamlines are directed outwards from the centre (Figure 7c). This streamline feature is a case of a Hopf bifurcation from bifurcation theory which suggests that the positive velocity gradient changes from to a negative gradient [5]. The direction of the lower vortex of the right cavity is the same as the case at 7.5L/min. The directions of the streamlines in the nasal valve region all flow from the outer wall to the septum wall. For particle deposition studies this feature is critical. Deposition of inhaled particles will be enhanced and should be expected to deposit onto the inner nasal septum wall side rather than on the outer surfaces. The complex flow in this nasal valve region therefore acts as a filtration device for particle deposition – a fact that is positive for toxic inhalation but a problem for drug delivery.

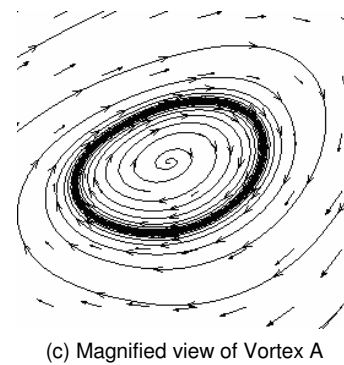
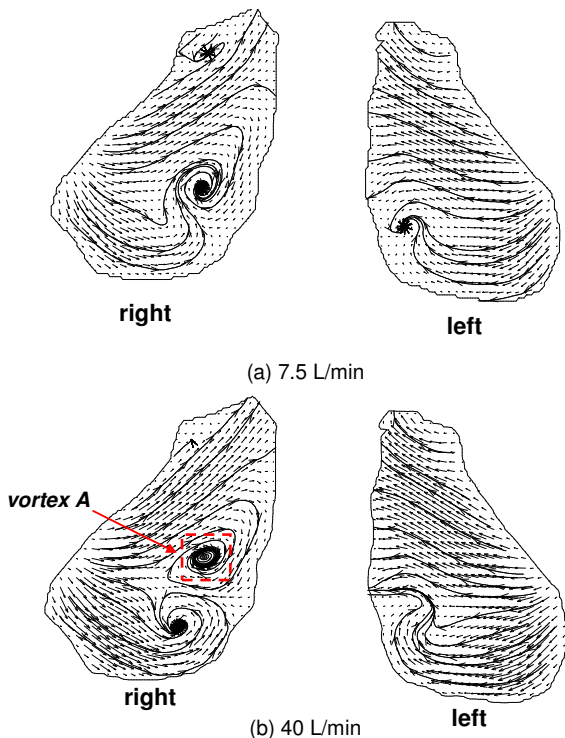


Figure 7. Velocity vectors and streamlines of cross-flow in the  $y$ - $z$  direction as well as streamlines in a cross-section in the nasal valve region as depicted in figure 1.

### Airflow Distribution

The flow distribution profiles for both flow rates are shown Figure 8. The profiles are similar where a maximum velocity of 1.0 m/s and 5.6 m/s for 7.5L/min and 40L/min respectively were found at the nasal valve region. After the maximum the flow steadily decreases due to the steady expansion of the cross-sectional area. The differences between the left and right cavities increase as the flow is increased which demonstrates that both the geometric configuration and the flow rate are important to the flow distribution inside the nasal cavity.

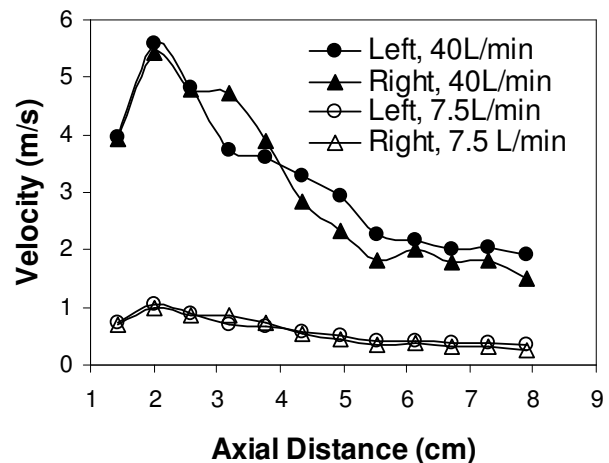


Figure 8. AverageFlow distributions in different cross-sections versus distance from anterior tip of nose.

### Turbinate Flow Distribution

The turbinate region consists of a narrow curled bone that protrudes into the main airway. The middle and inferior turbinate is an important structure for filtration and is thought to enhance heating and humidification where the mucosal wall surface area is increased. A cross-section of the mid-section of the turbinate region was subdivided into separate regions and labelled from A through to E which enabled measurement of the local distribution (Figure 9). Local volumetric flow was determined by integrating the velocity component normal to the plane over the cross-sectional area of each region. The results of airflow distribution at flow rates of 7.5 L/min and 40 L/min for left and right sides are given in Table 2 and 3, respectively. The  $\%Q_{Total}$  describes the proportion of flow as a percentage of the total flow rate.

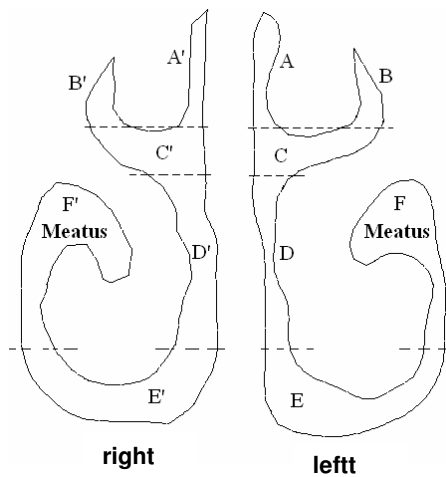


Figure 9. Coronal section locating various anatomical structures and airway. The section is located at 5.2 cm from the anterior tip of the nose.

	7.5L/min			40L/min			
	Area (%)	% $Q_{Total}$	$u$ (m/s)	$u_x$ (m/s)	% $Q_{tot}$	$u$ (m/s)	$u_x$ (m/s)
A	8.5	11.4	0.59	0.50	14.6	2.83	2.12
B	6.0	2.4	0.16	0.15	1.1	1.88	1.75
C	14.4	22.8	0.69	0.59	16.0	3.41	2.94
D	13.4	20.3	0.61	0.56	31.6	3.23	3.08
E	31.2	41.4	0.51	0.49	35.8	2.57	2.48
F	26.5	1.7	0.03	0.02	0.9	0.37	0.35

Table 2. Flow distribution on left side for different flow rates.

	7.5L/min			40L/min			
	Area (%)	% $Q_{Tot}$ al	$u$ (m/s)	$u_x$ (m/s)	% $Q_{tot}$	$u$ (m/s)	$u_x$ (m/s)
A'	5.5	2.1	0.16	0.12	4.3	1.57	1.26
B'	4.6	2.0	0.14	0.13	1.5	1.30	1.18
C'	15.4	29.1	0.67	0.60	31.7	2.76	2.48
D'	19.5	32.4	0.61	0.58	40.2	2.43	2.37
E'	26.7	32.5	0.37	0.35	21.8	2.32	2.24
F'	28.3	1.9	0.02	0.02	0.5	0.44	0.40

Table 3. Flow distribution on right side for different flow rates.

The flow analysis through the left cavity (Table 1) shows that 84% of the air passes through the superior medial airway (region C), the middle medial airway (region D) and the ventral medial airway (region E). These regions cover 59% of the entire cross-section. The right cavity is slightly wider and the regions C', D' and E' take up 61.6% of the right section. Despite the small difference in area coverage, region D in the left cavity has one constricting section which causes a higher resistance in the flow. The % $Q_{Total}$  for the regions C', D' and E' is 94%. The flow is therefore concentrated near the septum wall region and little flow reaches the outer regions in A, B and F. This brings into question the role of the turbinates to heat and humidify the air due to the increase in surface area of the meatus regions. Since only a small percentage of air reaches this outer meatus region

(F) the effectiveness of the heating and humidifying ability of the turbinates affects less than 2% of the flow field. The role of the turbinates may in fact be for different purposes such as to laminate or induce turbulence in the flow field. Further studies into this geometrical feature are therefore needed.

Overall the flow in the left cavity stays close to the wall while its distribution is mainly in the middle and more dominant in the lower sections while a small percentage of 14.6% is found in the upper section. This pattern was also observed in the work by Hahn et al. [6] and Keyhani et al. [11]. The right cavity shows less variation where the flow is concentrated within the middle sections. It was also found that the air flowing through in the X-direction (axial) component given by the velocity component  $u_x$  is very dominant which suggests that there is little secondary flows occurring.

The flow velocities are greater for the left cavity and this is accentuated when the flow rate is increased to 40L/min. Both cavities show the highest velocities occurring in region C. The flow in the left olfactory slit (zone A) is found to be larger than that of the right side (zone A'). This is a consequence of the flow of air in the left cavity which is divided by the constriction that is observed in the middle of region D. This constriction forces the flow to the upper and lower regions of the geometry. Additionally, region A is slightly greater in size than region A', which causes less resistance and allows the flow into this region. This flow feature may be considered as undesirable since it can lead to damage to the olfactory regions. Normally low flow characteristics are required in the olfactory region as it is a defense mechanism that prevents particles whose trajectories are heavily dependent on flow patterns from being deposited onto the sensitive olfactory nerve fibers, while vapors are allowed to diffuse for olfaction.

### Pressure Distributions

Figure 10 demonstrates the static pressure distribution in the nasal cavity. The average static pressure decreases as the distance from the anterior noses increases. Notably, increasing the flow rate causes a larger pressure drop. The static pressure is greater in the left cavity which suggests that the geometrical features on the left side leads to greater resistance. Such features may be greater curvature or small constrictions such as the one found in the turbinate region in Figure 8. The greatest resistance produced was found in the anterior 1.5–2.5 cm from the inlet. This result is a little different compared with Bridger and Procter et al. [1], which found that almost all of the nasal resistance to airflow is produced in the anterior 2–3 cm. It is mainly the deviation in the individual anatomic geometry caused the difference.

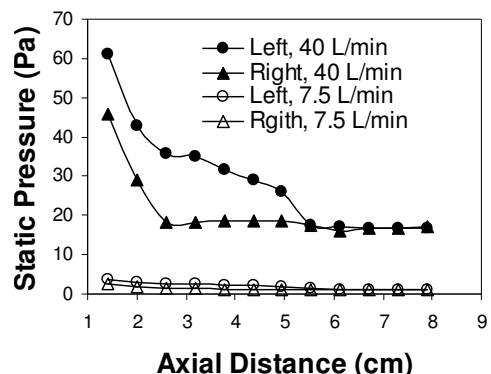


Figure 10. Average static pressure on different cross-sections versus axial distance.

## Conclusions

The human nasal cavity performs a variety of important physiological functions. Knowledge of the airflow patterns in the nasal cavity is essential to the prediction of gas-particle flows and also regional tissue exposure to inhaled air. The velocity and pressure distribution in human nasal cavity were investigated at constant flow rates of 7.5 L/min and exercise 40 L/min. It was found that air flow patterns are sensitive to the geometric construction within the human nasal cavity. For example the airflow distribution at a cross-section in the turbinate region found that a majority of the flow occurred along the floor of the airway and around the mid-height level for the left cavity. However for the right cavity the airflow was more evenly distributed from the top to the bottom. The key geometrical feature causing the difference was a small constriction found at the middle of the cross-section. This may lead to damage of the olfactory nerves due to an increase in the flow rate in the upper regions.

Maximum velocities were found at the narrowest cross-sections at the nasal valve region. Cross-sections within this region revealed complex vortices that are caused by the change of direction of the flow from vertical to horizontal as well as the complex geometry. The airflow distribution showed airflow remaining close to the nasal septum wall and little flow reached the outer meatus regions. This puts the role of the turbinates to heat and humidify the air under question and further investigations into this feature were recommended.

The results of this study presented detailed flow patterns and distribution of the air within the nasal cavity that provides complementary data to existing experimental data that often lack details. Additionally some critical health issues were revealed from the single airway geometry that was analysed. Further work is being undertaken to introduce particles to study the gas-particle dynamics.

## References

- [1] Bridger G.P., Procter D.F., Maximum Nasal Inspiratory Flow and Nasal Resistance. *Ann. Otol.*, **79**, 1970,481–488.
- [2] Bardina J. E., Huang P. G., and Coakley T. J., *Turbulence modeling validation, testing and development*, NASA-TM-110446,1997.
- [3] Cheng Y.S., Yeh H.C. and Guilmette R.A., Nasal Deposition of Ultrafine Particles in Human Volunteers and Its Relationship to Airway Geometry, *Aerosol Sci. Tech.*, **25**,1996, 274-291.
- [4] Churchill S.E., Shackelford L.L., Georgi J.N., and Black M.T., Morphological Variation and Airflow Dynamics in the Human Nose, *Am. J. of Hum. Biol.*, **16**,2004, 625–638.
- [5] Escudier M., Vortex Breakdown: Observations and Explanations, *Prog. Aerospace Sci.*, **25**,1988, 189-229.
- [6] Hahn I., Scherer P.W., and Mozell M.M., Velocity Profiles Measured for Airflow Through a Large-scale Model of the Human Nasal Cavity, *J. Appl. Physiol.*, **75**,1993, 2273-2287.
- [7] Haubermann S., Bailey A.G., Bailey M.R., Etherington G., Guilmette R.A., Youngman M.J., Influence of Anatomical Factors on Particle Deposition in the Nose, *J. Aerosol Sci.*,**31**, 2001,134-135.
- [8] Illum L., Transport of Drugs From the Nasal Cavity to the Central Nervous System, *Eur. J. Pharm. Sci.*, **11**,2000,1-18.
- [9] Inthavong K., Tian Z.F., Li H.F., Tu J.Y., Yang W., Xue C.L. and Li C.G., A Numerical Study of Spray Particle Deposition in a Human Nasal Cavity, *Aerosol Sci. Tech.*,**40**,2006,1034-1045.
- [10] Kelly J.T., Prasad A.k., and Wexler A.S., Detailed Flow Patterns in the Nasal Cavity, *J Appl. Physiol.*, **89**, 2000,323-337.
- [11] Keyhani K., Scherer P.W. and Mozell M.M., Numerical Simulation of Airflow in the Human Nasal Cavity, *J. Biomech Eng.*, **117**,1995,429-441.
- [12] Lindemann J., Keck T., Wiesmiller K., Sander B., Brambs H.J., Rettinger G., and Pless D., A Numerical Simulation of Intranasal Air Temperature during Inspiration, *Laryng.*, **114**, 2004, 1037-1041.
- [13] Naftali S., Rosenfeld M., Wolf M., and Elad D., The Air-Conditioning Capacity of the Human Nose, *Annals of Biomed. Eng.*, **33**, 2005. 545-553.
- [14] Pless D., M.S., Keck T., m.d., Weismiller K.M. et al., Numerical Simulation of Airflow Patterns and Air Temperature Distribution during Inspiration in a Nose Model with Septal Performance, *Am. J. Rhinol.*,**18**,2004,357-362.
- [15] Robert G. H., Forced Inspiratory Nasal Flow–volume Curves: A Simple Test of Nasal Airflow. *Mayo Clin. Proc.*, **76**, 2001, 990–994.
- [16] Schreck S., Sullivan K.J., Ho C.M. and Chang H.K., Correlations Between Flow Resistance and Geometry in a Model of the Human Nose, *J. Appl. Physiol.*, **75**, 1993,1767-1775.
- [17] Schroeter J. D., Kimbell J. S., Asgharian B., Analysis of Particle Deposition in the Turbinate and Olfactory Regions Using a Human Nasal Computational Fluid Dynamics Model, *J. Aerosol Med.*, **19**,2006,301-313.
- [18] Subramaniam R.P., Richardson R.B., Morgan K.T., Kimbell J. S. and Guilmette R.A., Computational Fluid Dynamics Simulations of Inspiratory Airflow in the Human Nose and Nasopharynx, *Inhal. Toxicol.*, **10**,1998,91–120.
- [19] Wang K., Jr.T.S.D., Morrison E.E., Vodyanoy V.J., *Numerical Simulation of Air Flow in the Human Nasal Cavity*, Proceeding of the 2005 IEEE, 2005,5607-5610.
- [20] Weinhold I. and Mlynski G., Numerical Simulation of Airflow in the Human Nose, *Eur. Arch. Otorhinolaryngol.*, **261**,2004, 452-455.
- [21] Wilcox D. C., *Turbulence Modelling for CFD*, DCW Industries, Inc., La Canada, California, 1998.
- [22] Zamankhan P., Ahmadi G., Wang Z., Hopke P.K., Cheng Y.S., Su W.C. and Lenoard D., Airflow and Deposition of Nano-particles in a Human Nasal Cavity, *Aerosol Sci. Tech.*,**40**,2006,463-476.